A Journal of the Gesellschaft Deutscher Chemiker

Angewandte International Edition GDCh Chemie

www.angewandte.org

Accepted Article

Title: Dual-Emissive Pt(II) Metallacage with Sensitive Oxygen Response for Imaging of Hypoxia and Imaging-Guided Chemotherapy

Authors: Huangtianzhi Zhu, Qi Li, Bingbing Shi, Fujing Ge, Yuezhou Liu, Zhengwei Mao, Hong Zhu, Sheng Wang, Guocan Yu, Feihe Huang, and Peter J. Stang

To be cited as: *Angew. Chem. Int. Ed.* 10.1002/anie.202009442

Link to VoR: https://doi.org/10.1002/anie.202009442

WILEY-VCH

RESEARCH ARTICLE WILEY-VCH

Dual-Emissive Pt(II) Metallacage with Sensitive Oxygen Response for Imaging of Hypoxia and Imaging-Guided Chemotherapy

Huangtianzhi Zhu,[a,b] Qi Li,[a,b] Bingbing Shi,[b] Fujing Ge,[d] Yuezhou Liu,[a] Zhengwei Mao,[e] Hong Zhu,[d] Sheng Wang,[c,*] Guocan Yu,[a,*] Feihe Huang[a,f,*] and Peter J. Stang[b,*]

[a] H. Zhu, Q. Li, Y. Liu, Dr. G. Yu, Prof. Dr. F. Huang
State Key Laboratory of Chemical Engineering, Center for Chemistry of High-Performance & Novel Materials, Department of Chemistry, Zhejiang University, Hangzhou 310027, P. R. China.
E-mail: fhuang@zju.edu.cn; guocanyu@zju.edu.cn
[b] H. Zhu, Q. Li, Dr. B. Shi, Prof. Dr. P. J. Stang
Department of Chemistry, University of Utah, Salt Lake City, Utah 84112, United States.
E-mail: stang@chem.utah.edu
[c] Prof. Dr. S. Wang
School of Life Sciences, Tianjin University and Tianjin Engineering Center of Micro-Nano Biomaterials and Detection-Treatment Technology, Tianjin 300072, P. R. China.
E-mail: shengwang@tju.edu.cn
[d] F. Ge, Prof. Dr. H. Zhu
College of Pharmaceutical Science, Zhejiang University, Hangzhou 310058, P. R. China.
[e] Prof. Dr. Z. Mao
MOE Key Laboratory of Macromolecular Synthesis and Functionalization, Department of Polymer Science and Engineering, Zhejiang University, Hangzhou 310027, P. R. China.
[f] Prof. Dr. F. Huang
Green Catalysis Center and College of Chemistry, Zhengzhou University, Zhengzhou 450001, P. R. China.

Supporting information for this article is given via a link at the end of the document.

Abstract: Imaging of hypoxia *in vivo* helps with accurate cancer diagnosis and evaluation of therapeutic outcomes. Here we report a Pt(II) metallacage with oxygen-responsive red phosphorescence and steady fluorescence for *in vivo* hypoxia imaging and chemotherapy. Intriguingly, the therapeutic agent and diagnostic probe are sophisticatedly integrated into the metallacage through heteroligation-directed self-assembly. Nanoformulation by encapsulating the metallacage into nanoparticles greatly enhance its stability in physiological environment, making the biomedical applications feasible. Apart from the enhanced red phosphorescence upon hypoxia, the ratio between red and blue emissions, which only varies with intracellular oxygen level, provides a more precise standard for hypoxia imaging and detection. Moreover, *in vivo* explorations demonstrate the promising potential applications of the metallacage-loaded nanoparticles as theranostic agents for tumor hypoxia imaging and chemotherapy.

Introduction

Intracellular oxygen (O_2) is essential for aerobic respiration that provides metabolic energy for living systems. Usually tissues with fast proliferation and metabolism, such as solid tumors, vascular diseases and brain abnormalities, can consume more O_2 that causes a hypoxia condition.[1,2] Therefore, detecting and imaging hypoxia in living cells are not only important for accurate cancer diagnosis but also very useful for the evaluation of therapeutic effects.[3] Up to now, many methods have been developed for sophisticated imaging methods of hypoxia, and two main approaches are involved. The first approach focuses on the detection of reductive enzymes including nitroreductase and azoreductase resulting from an enhanced reductive stress upon hypoxia by nitro- or azo-containing fluorophores.[4] Albeit showing selective response and easy preparation, the emission of the probe is irreversible due to bioreduction, which limits their further applications in reversibly monitoring the intracellular O_2 level. The second method employs phosphorescence probes showing dynamic emission varying with O_2 concentration.[5] Nevertheless, most of the phosphorescent probes are based on a mono-phosphorescent dye. The mono-emissive intensity is easily altered by the concentration of the probe and other biological conditions, with a relative lack of accuracy and reliability.[6] Consequently, for the demands of cancer diagnosis and potential treatments, it's important to develop new hypoxia probes with multiple emissions and phosphorescence characteristics.

Supramolecular coordination complexes (SCCs), which rely on the spontaneous self-assembly of metal acceptors and Lewis-basic organic ligands, have seen attention in order to mimic and study natural supramolecular assemblies.[7] In the past few decades, achievements have been made in coordination-driven self-assembly, from accurate assemblies of various Pt(II) metallacycles and metallacages, to multiple applications of these self-assemblies, typically in photophysics including cell imaging, optoelectronics and sensing.[8] Therefore, applying Pt(II) SCCs in hypoxia imaging is promising. Moreover, due to the directional coordination and charges of SCCs, the aggregation of ligands is prevented, which further promotes the accuracy of imaging by avoiding possible emission shifts upon aggregation of dyes.[9]

Herein, we report a Pt(II) metallacage (**1**) with dual-emissive and phosphorescent properties and its application in hypoxia imaging. Pt(II)-*meso*-tetra(4-carboxyphenyl)porphine was chosen as a phosphorescent ligand. This compound emits strong red phosphorescence with a long-lived triplet state in a deaerated atmosphere and the intensity is highly depended on O_2 concentration, hence a candidate as a sensitive O_2 probe.[10] However, this complex suffers from π-π stacking that weakens its emission,[11] and thus it's useful to use the metallacage to disperse it by taking advantage of the directional coordination

self-assembly. To achieve a dual-emissive property, the emission of the other ligand cannot be in the red region, and Förster resonance energy transfer (FRET) should also be avoided to sustain a steady fluorescence. Therefore, anthracene was selected as a blue fluorophore.[12] The combination of two ligands endows **1** with sensitive O_2-responsive red phosphorescence and steady blue fluorescence. The metallacage was also applied in hypoxia imaging *in vitro* and *in vivo*. Compared with traditional mono-emissive hypoxia probes, the metallacage not only shows reversible and sensitive O_2-reponsive phosphorescence but also provides a more reliable standard for hypoxia imaging and detection by calculating the ratio between red and blue emissions. For biomedical applications, an amphiphilic diblock copolymer is employed to encapsulate the metallacage to prepare a nanoparticulate formulation aiming to enhance the stability of the metallacage. Benefiting from the nanotechnology, the circulation time and tumor accumulation of the metallacage-loaded nanoparticles are significantly improved, which facilitate the optimization of the imaging and therapeutic performances. *In vivo* experiments demonstrate that the materials act as brilliant theranostic agents for tumor hypoxia imaging and chemotherapy, effectively suppressing the tumor growth with negligible side effects attributing to the enhanced permeability and retention effect. We anticipate that the sophisticated theranostic metallacage sensitive to tumor hypoxia can offer perspectives for enhanced molecular diagnostics and image-guided therapeutic applications.

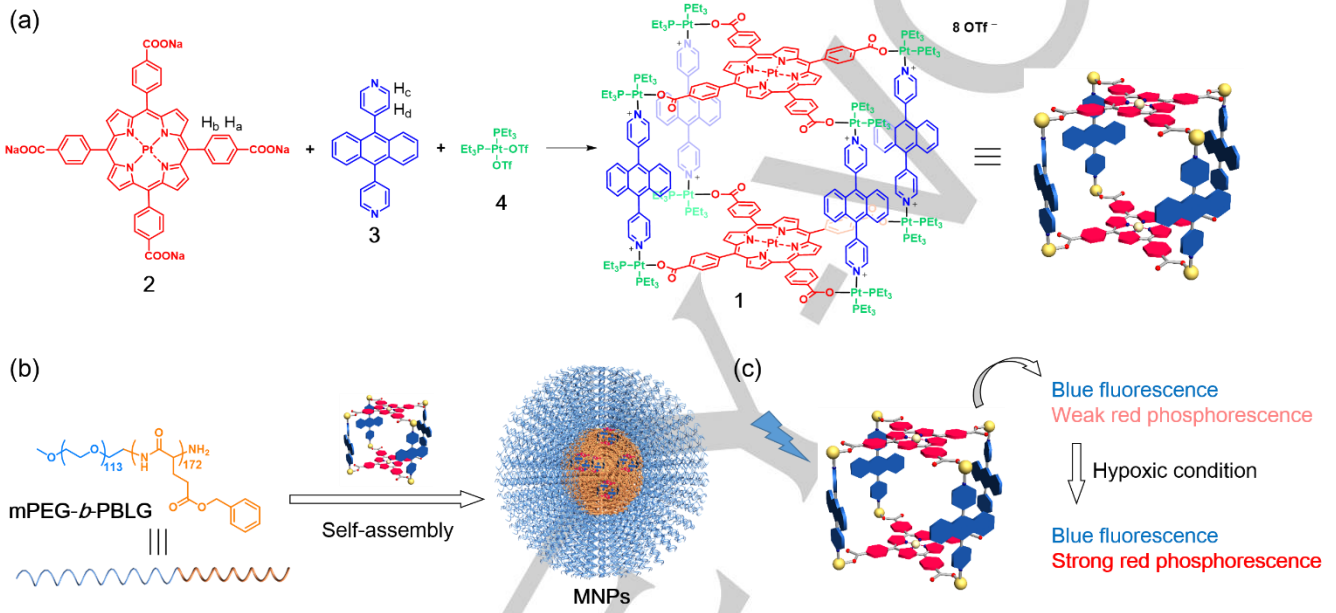

Scheme 1. Chemical structures and cartoon representations of (a) the preparation of **1**, (b) the formation of nanoparticles, and (c) the oxygen-responsive emission.

Results and Discussion

The metallacage **1** was prepared by a multicomponent self-assembly approach by stirring 9,10-di(pyridin-4-yl)anthracene (**2**), Pt(II) meso-tetra(4-carboxyphenyl)porphine sodium salt (**3**) and 90° Pt(II) acceptor (**4**) in a 2:1:4 ratio in a mixture of acetone/water (*v*/*v* = 4:1) at 70 °C for 8 h (Scheme 1). Metallacage **1** was identified by ^{1}H and ^{31}P{^{1}H} NMR spectroscopies (Figure 1a-d). In the ^{1}H NMR spectra, the peaks related to the protons on pyridyl groups of **2** shifted downfield after the cage formation, which agreed with the coordination of nitrogen atoms to the Pt(II) centers. The protons belonging to **3** matched the pre-designed ratio. The ^{31}P{^{1}H} NMR spectrum of **1** exhibited two doublet peaks with concomitant ^{195}Pt satellites, indicating two distinct phosphorus environments as required by a heteroligated coordination motif. These NMR results demonstrated the formation of a discrete and single-component structure with high asymmetry. The stoichiometry of **1** was examined by electrospray ionization time-of-flight mass spectrometry (ESI-TOF-MS, Figure 1e), whose results showed two peaks assigned to an intact moiety with 5+ charge states ascribed to the loss of OTf^- counterions (*m*/*z* = 1437.57 for $[M - 5OTf]^{5+}$ and *m*/*z* = 1471.96 for $[M - 4OTf + Na]^{5+}$). Three more peaks were also isotopically resolved and the results were consistent with their calculated distributions (Figure S5). All these data support the successful preparation of the metallacage.

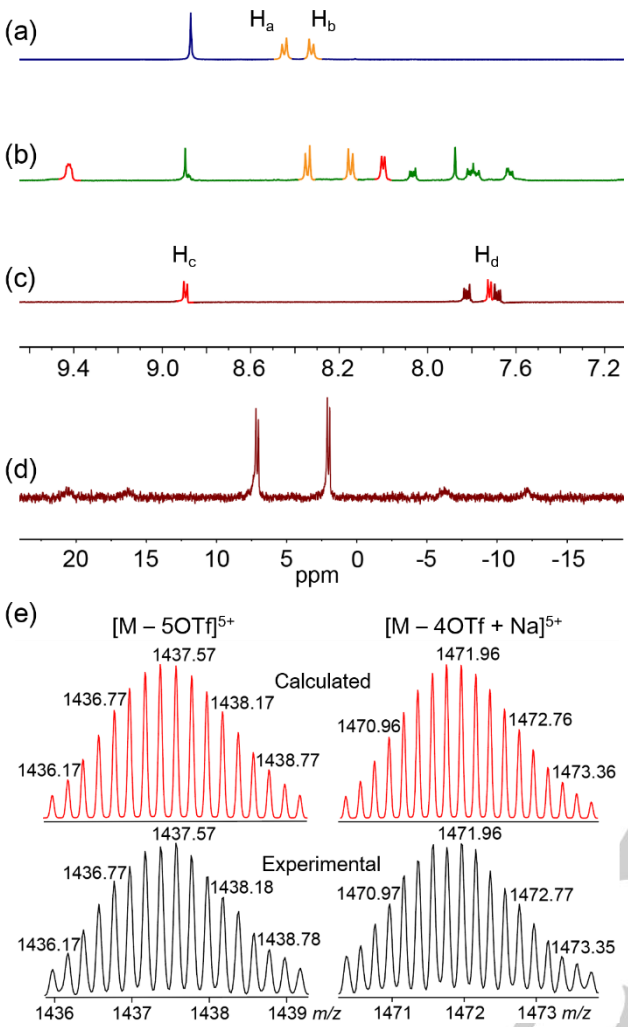

Figure 1. Partial ^{1}H NMR (500 MHz, acetone-d_6, 298 K) spectra of (a) **2**, (b) **1** and (c) **3**. (d) ^{31}P{^{1}H} NMR (121 MHz, acetone-d_6, 298 K) spectrum of **1**. (e) Calculated (red) and experimental (black) ESI-TOF-MS spectra of **1** (left: [M – 5OTf]$^{5+}$ charge state; right: [M – 4OTf + Na]$^{5+}$ charge state).

The photophysical properties of the metallacage **1** were explored. As shown in the UV-vis spectra, the overlap (Figure 2a) between absorptions of the ligands allowed exciting both dyes simultaneously. Moreover, after the formation of the metallacage, the bathochromic shift of the Soret band and the hypsochromic of the Q band were both found for **3** (Figure S7), indicating the prevented π-π stacking.[11,13] In the design principle, FRET was avoided, and this was verified by the negligible overlap between the fluorescent emission of **2** (maximum at 460 nm)[12] and the UV absorbance of **3** (maximum at 396 nm). The dual-emission property of **1** in a deaerated atmosphere was evaluated in fluorescence experiments. An acetone solution of the metallacage showed strong blue (420-480 nm) and very weak red (630-740 nm) emissions with 390 nm excitation. Upon purging with nitrogen, the red emission increased, which was a typical feature of phosphorescence, and thus led to a dual-emissive system (Figure 2b). The enhancement of the red emission was calculated to be more than 48 times in a nitrogen atmosphere, while the blue fluorescence only exhibited 0.30 times of an enhancement, illustrating that is a useful and sensitive O_2 probe with a tunable red phosphorescence and a nearly steady blue fluorescence. A similar change of the red phosphorescence was also found with the excitation wavelength at 510 nm (Figure 2c), and the promoted red phosphorescence was clearly seen by the naked eye (Figure 2d). Moreover, the red phosphorescence was reversible by exposure to O_2 (see the supplementary video). To further validate the phosphorescence property, a lifetime measurement of the emission at 660 nm was carried out and it was determined to be 30.1 μs (Figure S8), and this long lifetime proved the phosphorescence.[14]

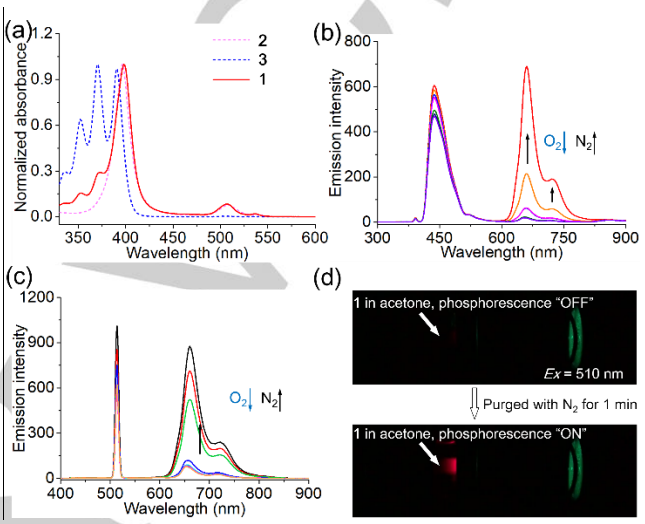

Figure 2. (a) Normalized UV-vis spectra of **1**, **2** and **3**. Fluorescence spectra of **1** with the excitations of (b) 390 nm and (c) 510 nm when purged with nitrogen bubbles. (d) Photos of the emissions of an acetone solution of **1** in a quartz cuvette in a fluorescence spectrometer with the excitations of 510 nm before and after purging. The concentration for each test was 1.00 mg/mL in acetone.

After understanding the dual-emissive and phosphorescent properties, we applied this metallacage in hypoxia imaging for probing the intracellular O_2 level. To improve the solubility and integrity of **1**, an amphiphilic polymer methylpoly(ethyleneglycol)-*block*-poly(*γ*-benzyl-*L*-glutamate) (**mPEG-*b*-PBLG**, Scheme 1) was used to encapsulate **1**.[15] **mPEG-*b*-PBLG** was prepared via ring-opening-polymerization (Scheme S3 and Figure S9). By using a co-precipitation method, **1** was encapsulated inside the self-assembled **mPEG-*b*-PBLG** to form metallacage-loaded nanoparticles (**MNPs**) with a loading efficiency of 65%. The morphology of **MNPs** were studied. As shown in Figure 3a, spherical **MNPs** were found with a diameter of ~150 nm on transmission electron microscope (TEM), which was in line with the result of dynamic light scattering (DLS, 134 ± 13.7 nm, Figure 3b). The zeta potential of the **MNPs** was also determined, revealing the neutral nature of **MNPs** benefiting from the PEGylation (Figure S10). These data indicate that the **MNPs** are favorable for cellular endocytosis.[16]

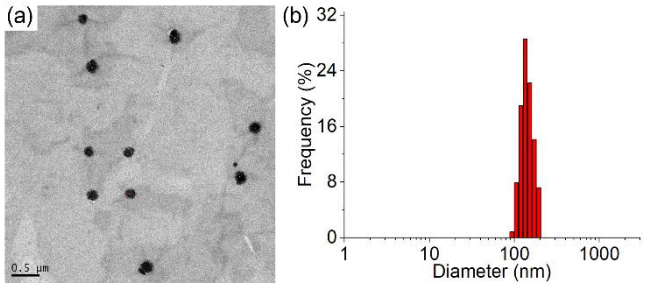

Figure 3. (a) TEM image of **MNPs**. The scale bar is 0.5 μm. (b) DLS result of **MNPs**.

With the reversible and sensitive O_2 response established, we further applied MNPs in hypoxia imaging to monitor the intracellular O_2 level. 4T1 breast cancer cells were chosen for hypoxia imaging due to their highly aggressive and fast proliferation characteristics. The endocytosis of MNPs by 4T1 cells was investigated. Inductively coupled plasma mass spectroscopy (ICP-MS) was chosen to monitor the intracellular platinum amount upon different incubation times. We found that the amount of intracellular platinum increased along with the incubation time and 182 ng platinum per million cells was achieved after 8 h incubation, indicating that MNPs were capable of intracellular accumulation (Figure 4a). For comparison, the endocytosis of cisplatin was also tested. According to the results of ICP-MS, MNPs exhibited slightly lower but sufficient uptake at every incubation time point compared with those of cisplatin likely arising from the fast diffusion of the small molecular weight compound. The biocompatibility of the polymeric carrier was evaluated by a 3-(4,5-dimethylthiazol-2-yl)-2,5-diphenyl tetrazolium bromide (MTT) assay. The relative cell viability of 4T1 cells after 48 h of incubation with different samples illustrated that the amphiphilic polymer mPEG-*b*-PBLG showed low cytotoxicity even at 200 μM (more than 87% of cells survived). The half-maximal inhibitory concentration (IC_{50}) value of **MNPs**, **1** and cisplatin were 8.58 ± 1.36, 4.50 ± 1.44 and 7.43 ± 1.34 μM, respectively (Figure 4b). The cytotoxicity of **MNPs** was attributed to the platinum-based ligand **4**, indicating that its anticancer efficacy was maintained by the formation of a metallacage.[17] Similar results were found when A549 (Figure 4c), HeLa and U87 cells (Figure S11) were employed.

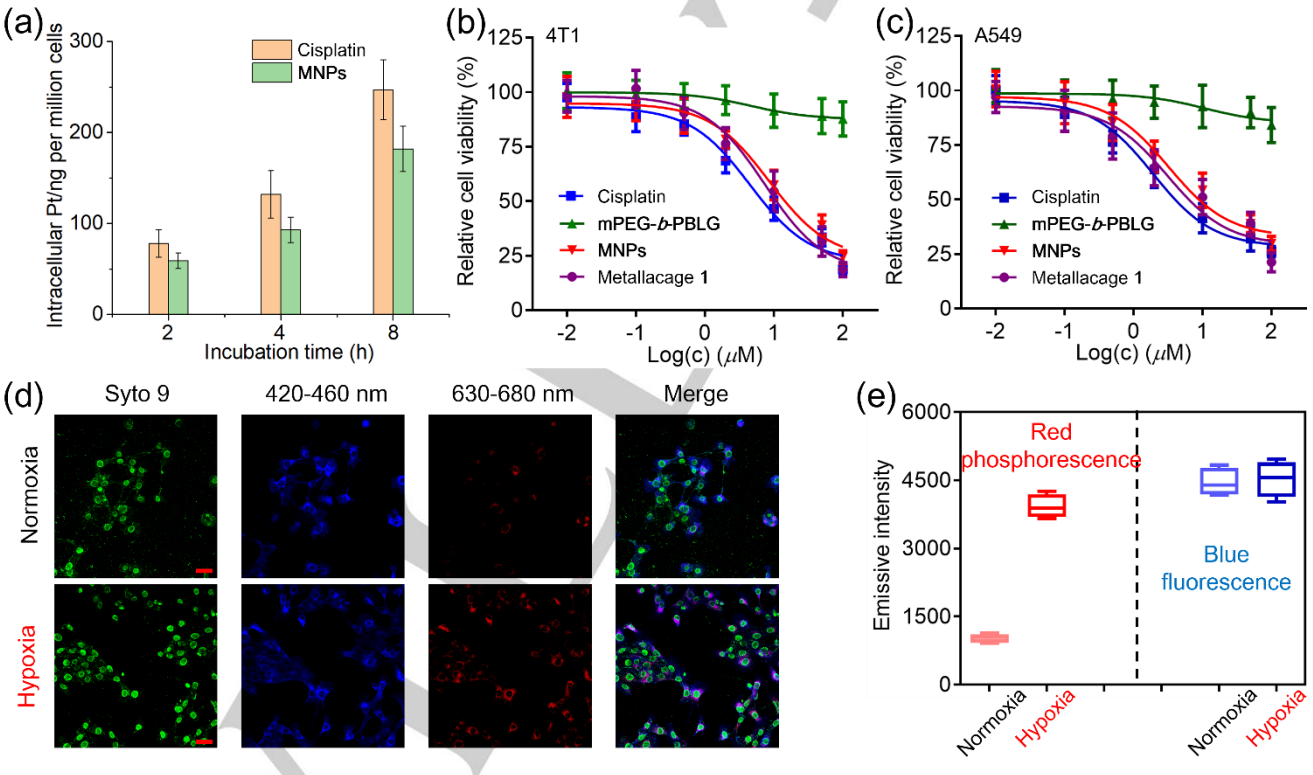

Figure 4. (a) ICP-MS results of intracellular Pt amount in 4T1 cells after incubation with **MNPs** or cisplatin for different times. Relative cell viabilities of (b) 4T1 and (c) A549 cells after treatment with different administrations. (d) CLSM images of 4T1 cells stained by Syto 9 (green, staining nucleus) and **MNPs** (blue and red) under normoxic (top) or hypoxic (bottom) conditions. (e) Quantitively emissive intensities of red phosphorescence and blue fluorescence in 4T1 cells under normoxic or hypoxic conditions.

After investigating the cytotoxicity of **MNPs**, hypoxia imaging experiments were performed. As shown in Figure 4d, the green and blue emissions were both recorded under the normoxia condition, whereas the red emission was barely detected. The blue emission perfused throughout the cells indicated that the uptake of **MNPs** was successful. By co-localization with green-emissive Syto 9, **MNPs** mainly distributed in the cytoplasm. In contrast with the images under the normoxia condition, 4T1 cells showed not only green/blue fluorescence but also red phosphorescence in the hypoxia condition. The increased red

emission under low O_2 concentration indicated the phosphorescence characteristic as well as the success of hypoxia imaging by the metallacage. Additionally, the merged image suggested that the blue and red emission are located identically, showing the dual-emissive property of **1** under the hypoxia condition. In order to illustrate the uniqueness of the metallacage, the intensities of blue and red emissions were quantitatively recorded (Figure 4e). We found that the red phosphorescence was increased by ~450% after the cells became hypoxic, while the blue fluorescence remained nearly stable, so that it could be a potential internal reference to quantify the intracellular O_2 level and detect hypoxia. The ratios between red phosphorescence and blue fluorescence were determined to be 0.224 and 0.866 upon normoxia and hypoxia, respectively. More importantly, the ratio only varies with the O_2 level. Compared with mono-emissive probes, which have different emissive intensities under different concentrations and endocytosis, the dual-emissive metallacage provides a more reliable standard for hypoxia detection and imaging.

In order to further explore the practical application of the metallacage in cancer theranostics, *in vivo* hypoxia imaging was firstly evaluated on 4T1 tumor-bearing mice. Prior to the hypoxia imaging studies, we assessed the pharmacokinetic data and time-dependent tissue distributions of **MNPs** using cisplatin as a control. The circulation time of **MNPs** and cisplatin were estimated by measuring the platinum amount in blood using ICP-MS spectroscopy at different time points after the injection of **MNPs**. As shown in Figure 5a, cisplatin was cleared from the blood quickly and the circulation half-life was estimated to be about 0.37 h. In contrast, the circulation half-life of **MNPs** was prolonged to 2.16 h, about 5.8-fold of cisplatin, referring to the time-dependent platinum amount in blood. Besides, the results of **MNPs** displayed a larger total area under the curve than that of cisplatin, indicating the improved circulation behavior of **MNPs**. The improved circulation time was ascribed to the stable nanoparticles and their hydrophilic exteriors that inhibited the protein adsorption. Furthermore, the biodistribution of **MNPs** and cisplatin in the tumor and other organs were determined (Figure 5b and c). According to the results of ICP-MS, the accumulation of cisplatin in the tumor was insufficient because of fast clearance, and the highest concentration of platinum was 2.8 ± 0.5 %ID/g (percent of dosage per gram organ/tissue). However, the intratumoral accumulation of **MNPs** was more feasible and the platinum concentration located in the tumor increased to 5.8 ± 0.8 %ID/g gradually after 24 h post injection resulting from the promoted circulation time of **MNPs**. Notably, the treatment with **MNPs** was able to retain a relatively higher level of intratumoral platinum amount (4.6 ± 0.7 %ID/g) even at 48 h post-injection. The extended circulation time and tumor accumulation implied **MNPs** were favorable for *in vivo* hypoxia imaging.

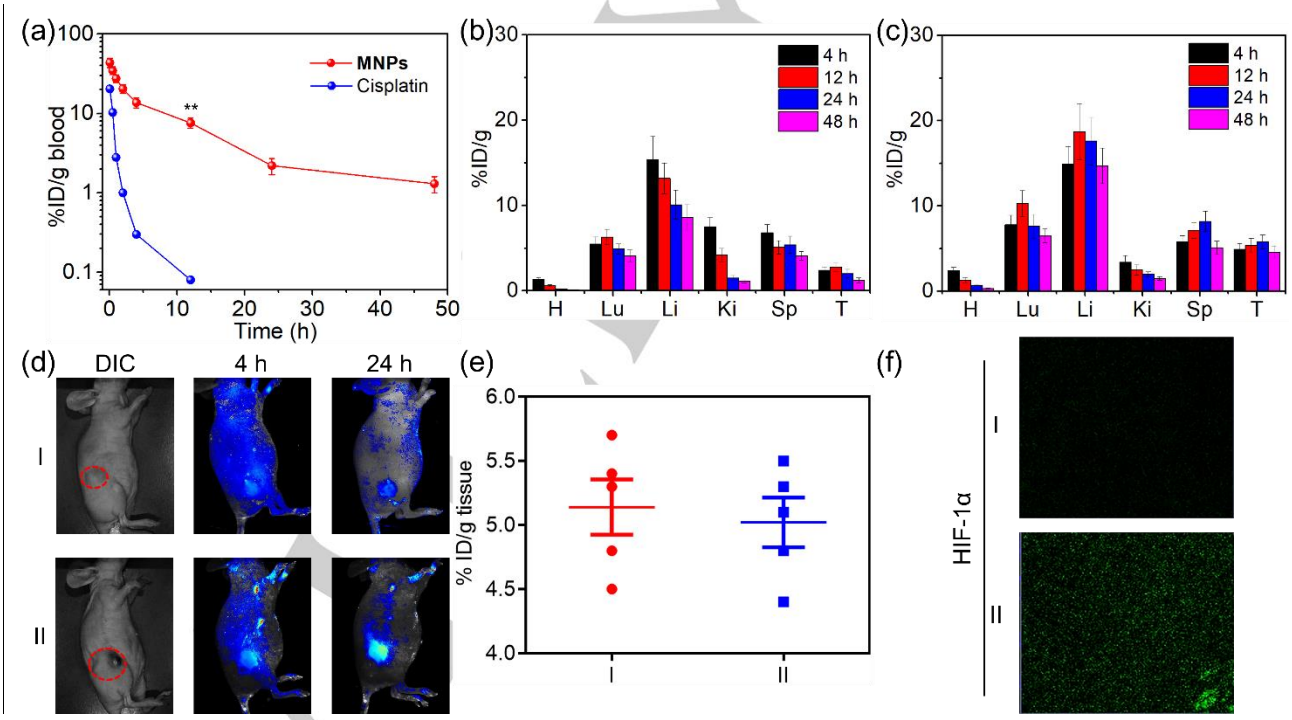

Figure 5. (a) Time-dependent Blood plasma amount of platinum after injecting **MNPs** and cisplatin. Tissue distributions of (b) cisplatin and (c) **MNPs** after injection. Organs: H, heart; Lu, lung; Li, liver; Ki, kidney; Sp, spleen; T, tumor. (d) *In vivo* fluorescent images of different sized tumor-bearing mice after the injection of **MNPs**. The signals were collected in the range of 600-800 nm with the excitation wavelength. (e) Intratumoral platinum amount of difference sized tumors at 24 h post *i.v.* injection of **MNPs**. (f) Immunofluorescence staining of tumor sections of difference sized tumors with an antibody to HIF-1α. Data are expressed as means ± s.d.

Due to the rapid oxygen consumption, poor vascularization and insufficient blood supply, the majority of solid tumors will develop hypoxia as they grow too large in size, which is responsible for resistances and tumor metastasis. It is reported that tumors in small size are relatively well vascularized and commonly display little or no hypoxic condition, while hypoxia

reappears in the characteristically perinecrotic distribution pattern when the tumors grow large.[18] Therefore, we chose two different sized 4T1 tumors (small tumor I, 100 mm^3; large tumor II, 360 mm^3) to illustrate the performance of hypoxia imaging under different intratumoral oxygen levels because larger tumors are usually more hypoxic that benefited brighter phosphorescence. *In vivo* hypoxia imaging was carried out after *i.v*. injection of **MNPs**, and whole body images were taken after 4 and 24 h post-injection by detecting emission in the range of 600-800 nm. As shown in Figure 5d, bright emissions were observed in tumor regions after 24 h post-injection, demonstrating the capability of *in vivo* hypoxia imaging for either small or large tumors. Besides, the emission shown in the large tumor possessed a better tumor-to-normal-tissue ratio and a stronger intensity than it in the small tumor, suggesting that **MNPs** exhibited a better performance when employed in large tumors. The stronger emission in large tumor was also consistent with the enhanced phosphorescence of metallacage **1** under a lower oxygen level in the large tumor. The intratumoral platinum amount was also measured by ICP-MS after completing hypoxia imaging in order to exclude the influence of the **MNPs** concentration. As shown in Figure 5e, the results of ICP-MS evidenced that the platinum amount in large tumors was slightly lower than those in relatively small tumors possibly caused by the poor vascularization in hypoxic tumor tissue. These data specified that the stronger emission was attributed to the more hypoxic condition rather than the higher **MNPs** concentration. Evidences for the hypoxic conditions in these tumors were found by monitoring the expression of hypoxia inducible factor 1α (HIF-1α). An immunofluorescence staining with an antibody to HIF-1α of tumor sections was involved and the results of staining showed a higher green emission in large tumors, which revealed the higher expression of the hypoxia-related marker and the more hypoxic condition in large tumors (Figure 5f). This conclusion agreed with the stronger emission of **MNPs** in large tumors that supported the practical potential of the metallacage in hypoxia imaging for cancer diagnosis.

cis-Pt(II) moieties are usually employed in antitumor drugs and the cytotoxicity of **MNPs** was also pointed out by aforementioned *in vitro* experiments. By combining the hypoxia imaging and antitumor capabilities, we conceived that it was possible to achieve cancer theranostics by **MNPs**. With the prolonged circulation time and tumor accumulation in hand, we subsequently evaluated *in vivo* antitumor efficiency of **MNPs** through 4T1 tumor-bearing mice. When the tumor volume reached near 90 mm^3, the mice were randomly divided into three groups and treated with (I) PBS, (II) free cisplatin and (III) **MNPs**, respectively. According to tumor inhibition curves (Figure 6a), the average tumor volume of mice injected with PBS increased rapidly. The mice administrated with cisplatin showed limited tumor inhibition mainly because of its relatively poor tumor accumulation and fast clearance. Excitingly, **MNPs** performed satisfactory therapeutic outcomes with a tumor inhibition rate of 79.6 % (Figure S12). The average tumor weight was calculated to be 1.50, 0.93, and 0.42 g at the end day of therapy for the mice dosed with PBS, cisplatin and **MNPs**, respectively, which was in accordance with the aforementioned therapeutic results. The excellent antitumor efficiency of **MNPs** was also supported by hematoxylin and eosin (H&E) staining (Figure 6b). Compared with the injections of PBS and cisplatin, the administration of **MNPs** led to severe apoptosis and necrosis in tumor.

Apart from the antitumor efficiency, the systemic toxicity of **MNPs** was also investigated. Blood from treated mice was collected for blood biochemistry tests in order to estimate the potential long-term systemic toxicity *in vivo* (Figure 6c-g). Compared with the blood sample from mice dosed with PBS, the level of alanine aminotransferase (ALT), aspartate aminotransferase (AST), blood urea nitrogen (BUN), creatinine (CREA) and alkaline phosphatase (ALP) all increased in the blood from mice injected with cisplatin, illustrating severe nephrotoxicity and hepatotoxicity. However, for the mice administrated with **MNPs**, no apparently abnormal parameter was found within the therapeutic period. Moreover, the monitoring of body weight changes also provided negligible weight loss for the MNPs-treated mice during the therapeutic period, whereas a weight loss appeared when employing cisplatin, indicating that **MNPs** had limited systemic toxicity due to the better tumor-specific distribution. Consequently, the aforementioned *in vivo* studies suggest that **MNPs** can be applied in theranostics with both hypoxia imaging and antitumor capabilities.

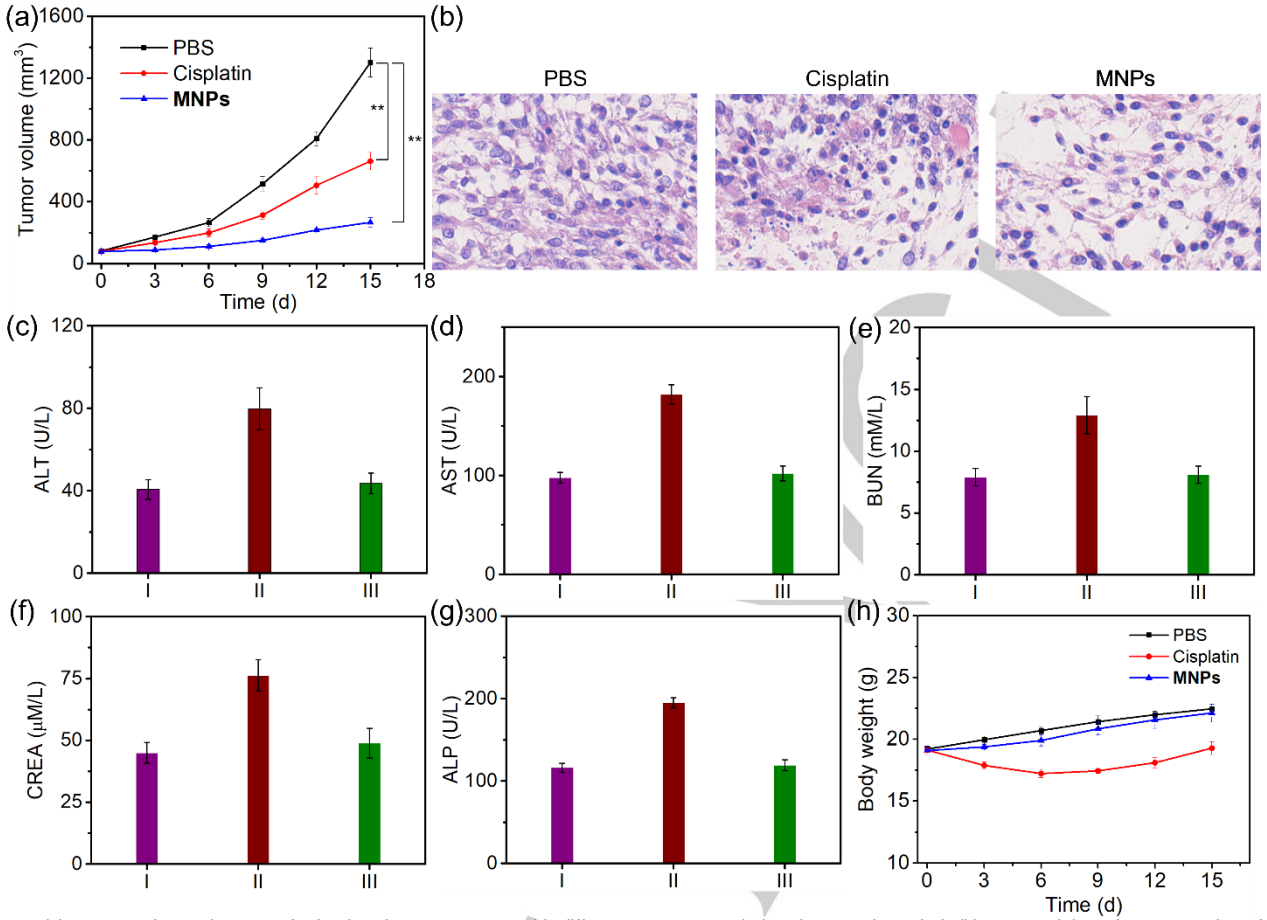

Figure 6. (a) Tumor volume changes of mice bearing 4T1 tumors with different treatments during therapeutic period. (b) H&E staining of tumor sections from mice bearing 4T1 tumors with different treatments. Blood biochemistry tests of (c) ALT, (d) AST, (e) BUN, (f) CREA and (g) ALP from mice treated with different formulations. I, PBS; II, cisplatin; III, **MNPs**. (h) Body weight changes of mice with different treatments. Data are expressed as means ± s.d.

Conclusion

In this work, we prepared a dual-emissive metallacage with blue fluorescence and red phosphorescence. The structure of the metallacage was investigated by NMR and MS spectroscopies. Benefited from the formation of metallacage, different ligands were able to be combined together by heteroligated coordinations, endowing the metallacage with the dual-emissive property. The red phosphorescence of the metallacage enhanced 48 times in a hypoxic condition, while the blue fluorescence nearly unchanged upon deaeration. After encapsulation by an amphiphilic polymer, the self-assembled nanoparticles showed a capability of hypoxia imaging by the phosphorescence increase along with the decrease of the intracellular O_2 level. Moreover, a more accurate hypoxia detection was achieved by using the ratio between red phosphorescence and steady blue fluorescence, suggested by *in vitro* experiments. Additionally, *in vivo* experiments revealed **MNPs** as a potential candidate in practicable theranostics that comprised both tumor hypoxia imaging and chemotherapy with improved circulation time and tumor accumulation. The high sensitivity, reliability and antitumor capability of this metallacage as a hypoxia probe with chemotherapy has wide future applications.

Acknowledgements

F.H. thanks the National Natural Science Foundation of China (21620102006) and the fundamental research funds for the central universities for financial support.

Keywords: supramolecular chemistry • self-assembly • metallacages • hypoxia imaging • theranostics

[1] (a) D. P. Jones, F. G. Kennedy. *Am. J. Physiol.* **1982**, *243*, 247–253; (b) E. Gnaiger, R. Steinlechner-Maran, G. Méndez, T. Eberl, R. Margreiter. *J Bioenerg Biomembr*, **1995**, *27*, 583–596.

[2] (a) A. L. Harris. *Nat. Rev. Cancer* **2002**, *2*, 38−47; (b) M. Hockel, K. Schlenger, B. Aral, M. Mitze, U. Schaffer, P. Vaupel. *Cancer Res.* **1996**, *56*, 4509−4515; (c) D. J. Heeger, D. Ress. *Nat. Rev. Neurosci.*, **2002**, *3*, 142−151.

[3] (a) X. Zheng, X. Wang, H. Mao, W. Wu, B. Liu, X. Jiang. *Nat. Commun.* **2015**, *6*, 5834; (b) A. S. E. Ljungkvist, J. Bussink, J. H. A. Kaanders, A. J. Van der Kogel. *Radiat. Res.* **2007**, *167*, 127–145; (c) K. Brindle. *Nat. Rev. Cancer*, **2008**, *8*, 94–107; (d) T.-X. Zhang, Z.-Z. Zhang, Y.-X. Yue, X.-Y. Hu, F. Huang, L. Shi, Y. Liu, D.-S. Guo. *Adv. Mater.* **2020**, *32*, 1908435.

[4] (a) T. W. Jacobs, A. M. Gown, H. Yaziji, M. J. Barnes, S. J. Schnitt. *Am. J. Clin. Pathol.* **2000**, *113*, 251–258; (b) T.-C. Cheng, S. R. Roffler, S.-C. Tzou, K.-H. Chuang, Y.-C. Su, C.-H. Chuang, C.-H. Kao, C.-S. Chen, I.-H. Harn, K.-Y. Liu, T.-L. Cheng, Y.-L. Leu. *J. Am. Chem. Soc.* **2012**, *134*, 3103–3110; (c) Y. Li, Y. Sun, J. Li, Q. Su, W. Yuan, Y. Dai, C. Han, Q. Wang, W. Feng, F. Li. *J. Am. Chem. Soc.* **2015**, *137*,

6407−6416; (d) W.-C. Geng, S. Jia, Z. Zheng, Z. Li, D. Ding, D.-S. Guo. *Angew. Chem.* **2019**, *131*, 2399−2403; *Angew. Chem. Int. Ed.* **2019**, *58*, 2377−2381.

[5] (a) X. Zheng, H. Mao, D. Huo, W. Wu, B. Liu, X. Jiang. *Nat. Biomed.l Eng.* **2017**, *1*, 0057; (b) Y.-E. L. Koo, Y. Cao, R. Kopelman, S. M. Koo, M. Brasuel, M. A. Philbert. *Anal. Chem.* **2004**, *76*, 2498−2505; (c) J.-N. Liu, W. Bu, J. Shi. *Chem. Rev.* **2017**, *117*, 6160−6224; (d) Y. Li, J. Liu, Z. Wang, J. Jin, Y. Liu, C. Chen, Z. Tang. *Adv. Mater.* **2020**, *32*, 1907718.

[6] Q. Zhao, X. Zhou, T. Cao, K. Y. Zhang, L. Yang, S. Liu, H. Liang, H. Yang, F. Li, W. Huang. *Chem. Sci.*, **2015**, *6*, 1825−1831.

[7] (a) M. Fujita, M. Tominaga, A. Hori, B. Therrien. *Acc. Chem. Res.* **2005**, *38*, 369–378; (b) T. R. Cook, Y.-R. Zheng, P. J. Stang. *Chem. Rev.* **2013**, *113*, 734 – 777; (c) D. A. Roberts, B. S. Pilgrim, G. Sirvinskaite, T. K. Ronson, J. R. Nitschke. *J. Am. Chem. Soc.* **2018**, *140*, 9616−9623.

[8] (a) M. L. Saha, X. Yan, P. J. Stang. *Acc. Chem. Res.* **2016**, *49*, 2527−2539; (b) X. Yan, T. R. Cook, P. Wang, F. Haung, P. J. Stang. *Nat. Chem.* **2015**, *7*, 342–348; (c) Q. Zhang, D. Tang, J. Zhang, R. Ni, L. Xu, T. He, X. Lin, X. Li, H. Qiu, S. Yin, P. J. Stang. *J. Am. Chem. Soc.* **2019**, *141*, 17909–17917; (d) M. Zhang, S. Li, X. Yan, Z. Zhou, M. L. Saha, Y.-C. Wang, P. J. Stang. *Proc. Natl. Acad. Sci. U. S. A.* 2016, *113*, 11100−11105.

[9] (a) T. R. Cook, Y.-R. Zhang, P. J. Stang. *Chem. Rev.* **2013**, *113*, 734–777; (b) Y. Sun, Y. Yao, H. Wang, W. Fu, C. Chen, M. L. Saha, M. Zhang, S. Datta, Z. Zhou, H. Yu, X. Li, P. J. Stang. *J. Am. Chem. Soc.* **2018**, *140*, 12819−12828.

[10] (a) R. Xu, Y. Wang, X. Duan, K. Lu, D. Micheroni, A. Hu, W. Lin. *J. Am. Chem. Soc.* **2016**, *138*, 2158−2161; (b) X.-D. Wang, J. A. Stolwijk, T. Lang, M. Sperber, R. J. Meier, J. Wegener, O. S. Wolfbeis. *J. Am. Chem. Soc.* **2012**, *134*, 17011−17014; (c) J. Yang, Z. Wang, Y. Li, Q. Zhuang, J. Gu. *Chem. Mater.* **2016**, *28*, 2652−2658.

[11] V. V. Vasil'ev, S. M. Borisov, Y. O. Chubarova, V. D. Rumyantseva *Russ. J. Inorg. Chem.*, **2003**, *48*, 385–390.

[12] S. I. Vasylevskyi, D. M. Bassani, K. M. Fromm. *Inorg. Chem.* **2019**, *58*, 5646−5653.

[13] (a) G. Yu, S. Yu, M. L. Saha, J. Zhou, T. R. Cook, B. C. Yung, J. Chen, Z. Mao, F. Zhang, Z. Zhou, Y. Liu, L. Shao, S. Wang, C. Gao, F. Huang, P. J. Stang, X. Chen. *Nat. Commun.* **2018**, *9*, 4335; (b) H. Zhu, H. Wang, B. Shi, L. Shangguan, W. Tong, G. Yu, Z. Mao, F. Huang. *Nat. Commun.* **2019**, *10*, 2412.

[14] (a) E. Onal, S. Sab, J. Hurpin, K. Ertekin, S. Z. Topal, M. U. Kumke, C. Hirel. *J. Fluoresc.* **2017**, *27*, 861–868; (b) Z. Lv, L. Zou, H. Wei, S. Liu, W. Huang, Q. Zhao. *ACS Appl. Mater. Interfaces* **2018**, *10*, 19523−19533.

[15] C. Cai, W. Zhu, T. Chen, J. Lin, X. Tian. *J. Polym. Sci. Pol. Chem.* **2009**, *47*, 5967–5978.

[16] J. Panyam, V. Labhasetwar. *Adv. Drug Deliv. Rev.*, **2003**, *55*, 329–347.

[17] (a) D. Wang, S. J. Lippard. *Nat. Rev. Drug Discov.* **2005**, *4*, 307–320; (b) X. Wang, Z. Guo. *Chem. Soc. Rev.* **2013**, *42*, 202–224.

[18] X.-F. Li, J. A. O'Donoghue. *Cancer Lett.* **2008**, *264*, 172-180.

10.1002/anie.202009442

Entry for the Table of Contents

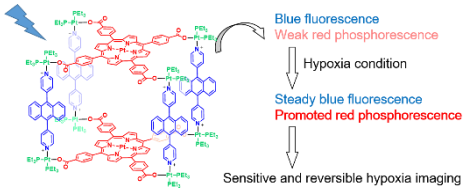

Imaging of hypoxia *in vivo* helps with accurate cancer diagnosis and evaluation of therapeutic outcomes. Here we report a Pt(II) metallacage with oxygen-responsive red phosphorescence and steady fluorescence for *in vivo* hypoxia imaging and chemotherapy.